Influence of particle-fluid density ratio on the dynamics of finite-size particles in homogeneous isotropic turbulent flows

Jie Shen[*] and Zhiming Lu[†]
School of Mechanics and Engineering Science, Shanghai Institute of Applied Mathematics and Mechanics, Shanghai University, Shanghai 200072, China

Lian-Ping Wang[‡]
Guangdong Provincial Key Laboratory of Turbulence Research and Applications, Center for Complex Flows and Soft Matter Research and Department of Mechanics and Aerospace Engineering, Southern University of Science and Technology, Shenzhen 518055, Guangdong, China and Department of Mechanical Engineering, 126 Spencer Laboratory, University of Delaware, Newark, Delaware 19716-3140, USA

Cheng Peng[§]
Key Laboratory of High Efficiency and Clean Mechanical Manufacture, Ministry of Education, School of Mechanical Engineering, Shandong University, Jinan 250061, China and National Demonstration Center for Experimental Mechanical Engineering Education, Shandong University, Jinan 250061, China

(Received 12 March 2021; revised 10 June 2021; accepted 30 July 2021; published 26 August 2021)

In this paper, direct numerical simulations of particle-laden homogeneous isotropic turbulence are performed using lattice Boltzmann method incorporating interpolated bounce-back scheme. Four different particle-fluid density ratios are considered to explore how particles with different particle-fluid density ratios respond to the turbulence. Overall particle dynamics in the homogeneous isotropic turbulence such as the Lagrangian statistics of single particle and the preferential concentration of particles are investigated. Results show that particle acceleration and angular acceleration are more intermittent than velocity and angular velocity for finite-size particles with different particle-fluid density ratios. The preferential concentration of particles is investigated using radial distribution function and Voronoï tessellation, and the preferential concentration is more profound for particles with two intermediate particle-fluid density ratios. The Voronoï analysis indicates that the distribution of Voronoï cells satisfy the log-normal distribution better than the gamma distribution. The mechanism of preferential concentration is analyzed using the sweep-stick mechanism and drift mechanism. Results show that although a higher probability of having particles located near the sticky points is found, the sticky mechanism is very weak for large density ratios. The particle clustering is then found to be better qualitatively described by the drift mechanism.

DOI: 10.1103/PhysRevE.104.025109

I. INTRODUCTION

Particle-laden flows are ubiquitous in numerous environmental and industrial processes including dust and haze transport, warm rain formation and particle coalescence in fluidized bed reactors, etc. [1,2] Understanding how particles respond to the carrier flow can help us better predict natural and engineering phenomena such as particle dispersion and accumulation. Theoretical analysis of particle motion is usually based on the approximation that the particle size is much smaller than the smallest flow scale (Kolmogorov scale), such approximation is known as the point particle approximation [3,4], which is also frequently adopted in numerical simulation [5]. However, when the particle size is of or larger than the Kolmogorov scale, the point particle approximation is no longer accurate as the force exerted on the particle is poorly understood and the interaction between the two phases can no longer be accurately treated by the point particle approach [6]. Compared to the literatures considering point particle approximation, relative fewer studies consider particles with the size larger than the Kolmogorov scale in a turbulent flow, but increasing attention is attracted to explore the finite-size effect of particles (see Tenneti and Subramaniam [7], and reference therein). In general, experiments on turbulent two-phase flows are challenging as a result of optical limitation and difficulty in three dimensional particle detection technology, especially when the volume fraction of solid phase increases. There are a few experimental studies on the dynamics of finite-size

[*]jieshen@shu.edu.cn
[†]Corresponding author: zmlu@shu.edu.cn
[‡]wanglp@sustech.edu.cn
[§]pengcheng@sdu.edu.cn

particles, such as the work investigating particle acceleration by Qureshi *et al.* [8,9] and the work investigating particle spatial distribution by Fiabane *et al.* [10].

With the development of computing resources, numerical simulations provide an alternative way to help explore the influence of carrier phase on the particle statistics and the modulation of turbulence due to the presence of finite-size particles. For point particle simulation, the Fáxen correction has been used to account for the finite-size effect of particles [11]. However, it is usually difficult to establish the undisturbed ambient flow in the absence of particles, especially when the particle size is larger than the Kolmogorov scale of the carrier flow. The fully resolved simulation is a better way to incorporate the interphase coupling in the particle-laden flow. For fully resolved simulation of turbulence laden with finite-size particles, the main challenge is how to resolve the particle-fluid interface precisely, much effort has been devoted to treat no-slip boundary condition on particle surface with a relatively sharp interface. A comprehensive review regarding the numerical methods can be found in the review paper of Maxey [12]. Among the methods enforcing no-slip boundary condition, two most widely used methods are immersed boundary method (IBM) [13] and bounce-back scheme in lattice Boltzmann method (LBM) [14–17] due to their simplicity and efficiency.

Homogeneous isotropic turbulence is an idealized and simplified model suitable for investigating the particle dynamics in turbulence, a brief review is given here on the literatures of particle dynamics in homogeneous isotropic turbulence. Among the researches of finite-size particles in homogeneous isotropic turbulence, one of the scientific concerns is the acceleration of finite-size particles in turbulence. Qureshi *et al.* [8] experimentally studied the acceleration of different finite-size particles and found that the distribution of acceleration was consistent with the empirical log-normal like distribution proposed by by Mordant *et al.* [18] for tracer particles but with slightly different fitting parameters. The work was extended to finite-size particles with largest particle-fluid density ratio up to 65 later [9], and a negligible influence of particle-fluid density ratio on normalized particle acceleration distribution was observed. Calzavarini *et al.* [11] investigated the finite-size particle acceleration property using point particle approach with Fáxen correction, and found correct trend of particle acceleration PDF as in Qureshi *et al.* [8,9]. Yeo *et al.* [19] numerically studied the velocity and acceleration statistics of finite-size particles with particle-fluid density ratio close to unity in homogeneous isotropic turbulence, in which the flow field is solved using pseudo-spectral method and particle-fluid interface is handled using force coupling method. Similar observation for particle acceleration with Qureshi *et al.* [8] was found. Homann *et al.* [20] investigated the motion of a single neutrally buoyant particle in homogeneous isotropic turbulence by pseudo-penalization method. It was found that the distribution of particle acceleration was in good agreement with the empirical equation proposed by Qureshi [8]. But whether this empirical equation is true for even larger particle-fluid density ratio is unclear.

Another important scientific concern is the particle spatial distribution. Many studies have shown that point particles heavier than fluid accumulate in local high strain rate region and bubbles accumulate in the vortical region [21]. The accumulation of point particles is known as the preferential concentration which is most remarkable when the Stokes number St defined as the ratio of particle relaxation time τ_p ($\tau_p = \frac{d_p^2 \rho_p}{18 \nu \rho_f}$) and Kolmogorov time scale of the turbulence τ_k ($\tau_k = (\nu^3/\epsilon)^{1/2}$) is of the order unity [22–24]. However, limited understanding of preferential concentration for finite-size particles is available. Fiabane *et al.* [10] studied the preferential concentration of finite-size particles with two different particle-fluid density ratios (neutrally buoyant and 2.5) by experiment. The Stokes number was controlled by adjusting the intensity of turbulence and was kept of the order unity in the experiment, no preferential concentration was observed for neutrally buoyant particles whereas heavy particles formed clusters. Uhlmann *et al.* [25] studied the preferential concentration of particles with two different sizes and with density ratio fixed at 1.5, where finite difference method incorporating with IBM was used in the simulation. It was found that the sweep-sticky mechanism proposed by Goto and Vassilicos [26] for point particles can be used to explain the particle accumulation location for finite-size particles in their work. The sweep-sticky mechanism establishes a link between the accumulation of point particles and the local properties of the fluid acceleration field, and the particles tend to accumulate in the regions where the divergence of fluid acceleration is larger than 0. Wang *et al.* [27] considered the van der Waals force in the simulation using LBM with bounce-back scheme and found a more profound preferential concentration. From the literatures above, we can see that St alone is insufficient to characterize the nonuniform spatial distribution of particles of finite size and particle-fluid density ratio is indeed an important parameter for particle dynamics in particle-laden turbulent flow. We are also interested in whether the sweep-sticky mechanism is valid for finite-size particles at a large particle-fluid density ratio, and whether other mechanism can properly explain the particle clustering when the sweep-sticky mechanism is invalid, such as the drift mechanism proposed by Bragg *et al.* [28,29].

In general, the influence of turbulence on particle dynamics is not well understood for finite-size particles especially particles with different particle-fluid density ratio, the researches in the literature mentioned above mainly focus on the effect of sizes, the particle-fluid density ratio which is another important parameter is limited to unity or close to unity and the understanding of influence from particle-fluid density ratio is still limited. In this paper, we aim to investigate the influence of particle-fluid density ratio on the motion and spatial distribution of particles in turbulence. The homogeneous isotropic turbulence is chosen, and the gravity is excluded in this study to concentrate on the effect of particle-fluid density ratio itself on particle dynamics. The lattice Boltzmann method is used in this study due to its flexibility in treating solid boundaries around particles and its high parallel-computation performance. Several different strategy of bounce-back schemes [15–17] and the short range interaction model [30] are used to reproduce the physics behind as faithfully as possible. The code has been applied to and validated in different particulate flows, such as decaying turbulence [31], homogeneous isotropic turbulence [32], and turbulent channel flow [33].

The paper is organized as follows. The method we use in the simulation is briefly introduced in Sec. II. The simulation parameters and results are given in Sec. III. Finally, a summary is provided in Sec. IV.

II. THE NUMERICAL METHOD

The flow field is solved using the lattice Boltzmann method (LBM) in this paper. Instead of solving the Navier-Stokes (N-S) equations, LBM is a mesoscopic method which tracks the evolution of molecular distribution functions. The Navier Stokes equations can be recovered through the Chapmann-Enskog expansion of lattice Boltzmann equation (LBE). The macroscopic variables such as pressure and velocity are obtained from the moments of molecular distribution functions. For numerical stability, the multiple relaxation time (MRT) collision model [34] is chosen in this study. The evolution equation with the MRT collision model is

$$f_\alpha(\boldsymbol{x}+\boldsymbol{e_\alpha}\delta\boldsymbol{t}, t+\delta t) - f_\alpha(\boldsymbol{x}, t) = -\boldsymbol{M}^{-1}\boldsymbol{S}[\boldsymbol{m}(\boldsymbol{x}, t) - \boldsymbol{m}^{(\mathrm{eq})}(\boldsymbol{x}, t)] + \boldsymbol{M}^{-1}\boldsymbol{\Psi}, \quad (1)$$

where $f_\alpha(\boldsymbol{x}, t)$ is the distribution function located at space location $\boldsymbol{x}$ at time t, $\boldsymbol{e_\alpha}$ is the discrete velocity (a D3Q19, three-dimensional 19 discrete velocities, is used in this paper), $\boldsymbol{M}$ is the transformation matrix converting the distribution function f to moment space $\boldsymbol{m}$. $\boldsymbol{S}$ is a diagonal relaxation matrix specifies the relaxation parameters for different moments $\boldsymbol{m}$. $\boldsymbol{\Psi}$ is the mesoscopic forcing term which realize the body force in the macroscopic N-S equations. The right-hand side of Eq. (1) is known as the collision operator, $\boldsymbol{\Omega_i} = -\boldsymbol{M}^{-1}\boldsymbol{S}[\boldsymbol{m}(\boldsymbol{x}, t) - \boldsymbol{m}^{(eq)}(\boldsymbol{x}, t)] + \boldsymbol{M}^{-1}\boldsymbol{\Psi}$. The LBM scheme is usually divided into two steps, known as the collision step $[f^*_\alpha(\boldsymbol{x}, t) = f_\alpha(\boldsymbol{x}, t) + \boldsymbol{\Omega_i}]$ and the streaming step $[f_\alpha(\boldsymbol{x} + \boldsymbol{e_\alpha}\delta\boldsymbol{t}, t+\delta t) = f^*_\alpha(\boldsymbol{x}, t)]$. The well-known stochastic forcing scheme of Eswaran and Pope [35] is applied to drive the turbulent flow. With the random forcing scheme, the average net rate of energy input which is balanced by the dissipation rate can be estimated as

$$\text{Rate of energy input} = \frac{4N_f\sigma_f^2 T_f}{1 + T_f\left(\sigma_f^2 T_f N_f k_0^2\right)^{1/3}/\beta}, \quad (2)$$

where N_f is the number of modes forced, k_0 is the lowest wave number in spectral units, σ_f and T_f are the forcing amplitude and timescale, respectively, $\beta \approx 0.8$ based on the lower resolution simulation of Eswaran and Pope [35].

The no slip boundary between the particle-fluid interface is achieved by the interpolated bounce-back scheme to ensure the sharp interface between two phases. Figure 1 is a sketch of the bounce-back scheme in two dimensions, the black vectors represent the known molecular distribution functions corresponding to the discrete velocities in these directions which are propagated from the neighboring fluid nodes during streaming step, and the red vectors are unknown molecular distribution functions as the nodes where these distributions are propagated from are in the solid phase. The unknown distributions in the streaming step are obtained using the interpolated bounce-back scheme. The default interpolated bounce-back scheme used is proposed by Bouzidi *et al.* [15] which requires two other nodes on the fluid phase. The single-point second-order accuracy bounce back proposed by Zhao and Yong [16] is adopted when the distance between two particles is too small and only one fluid node is available. These two schemes both have a second-order accuracy and maintain a low numerical dissipation for the solid boundary condition. The hydrodynamic force and torque acting on the particles are calculated by integrating the momentum and moment of momentum exchange over the particle surface during interpolated bounce-back process. According to Newton's second law, the translational velocity and angular velocity of each particle can be updated after the hydrodynamic force and torque are obtained, and the position of each particle can be updated afterwards. A new fluid point which is occupied by the particle before the update of particle position may occur after the movement of a particle, the unknown new fluid node is refilled by the 'equilibrium and nonequilibrium' extrapolation scheme [36]. As the current particle-laden system is far beyond the dilute limit, the particle-particle interactions must be taken into account. The lubrication force model suggested by Brndle de Motta *et al.* [30] is selected to deal with the short range hydrodynamic interactions when the spacing between two particles is within one lattice node. When the particles are in contact, the soft-sphere collision model is used to avoid nonphysical overlapping between particles [30]. More details about the D3Q19 MRT-LBM model incorporating interpolated bounce-back scheme can be found in the references listed above and [27,31–33].

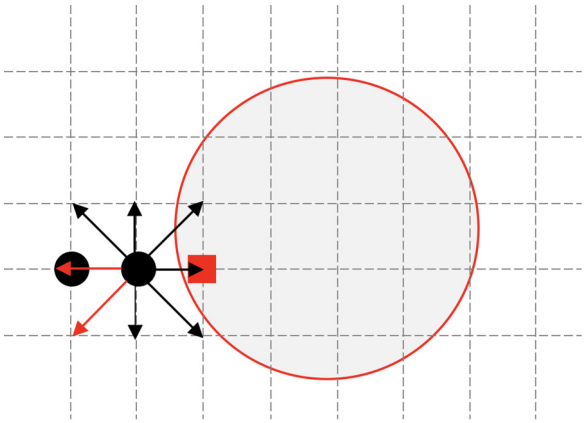

FIG. 1. A two-dimensional sketch of the bounce-back scheme. The red circle is the particle surface, the black spheres are the fluid nodes, the red squares are the solid nodes, the black vectors represent the known molecular distribution functions during streaming step and the red vectors are the unknown molecular distribution functions which are determined using interpolated bounce-back scheme. The interpolated bounce-back scheme uses different number of fluid nodes to construct the unknown distributions in different situations.

III. SIMULATION SETUP AND RESULTS

The homogeneous isotropic turbulence is performed in a cubic domain with periodic boundary in all three directions. To exclude the additional energy injection induced by gravity and focus on the influence of particle-fluid density ratio, gravity is neglected in this work. The single-phase flow driven by the random force was simulated first before the particles

TABLE I. Time-averaged flow statistics in single-phase and particle-laden homogeneous isotropic turbulence. SP denotes single-phase homogeneous isotropic turbulence. $\rho^* = \rho_p/\rho_f$ is the particle-fluid density ratio.

	SP	Case 1 $\rho^* = 1$	Case 2 $\rho^* = 5$	Case 3 $\rho^* = 20$	Case 4 $\rho^* = 100$
Re_λ	76.49	72.28	64.97	42.79	31.37
η_k	0.90	0.96	0.94	0.96	1.00
λ	15.55	16.01	14.98	12.65	10.99
u'	3.92E-2	3.63E-2	3.46E-2	2.66E-2	2.28E-2
ε	7.77E-7	6.26E-7	6.51E-7	5.61E-7	7.65E-7
L_E	79.39	77.34	64.93	37.60	23.07
τ_k	100.81	113.20	110.05	118.71	122.86
τ_E	1.99E3	2.11E3	1.85E3	1.36E3	9.94E2
Skewness	−4.87E-1	−4.95E-1	−4.97E-1	−4.69E-1	−4.90E-1
Flatness	4.81	5.88	8.92	13.44	17.12
St		4.39	21.95	87.79	439.96

are introduced. When the single-phase flow reaches stationary, solid particles are inserted into the flow. The particle diameter is eight times the lattice spacing which corresponds to 8.8 times the Kolmogorov length scale at the particle release time and the simulation domain is 32 times the particle size which corresponds to a grid resolution of 256^3. The resolution requirement has been discussed previously in Wang *et al.* [32], to produce reliable flow statistics when compared with the pseudospectral method. Four different particle-fluid density ratios, 1, 5, 20, and 100, are investigated, which represents the neutrally buoyant particles, two types of intermediate density particles and heavy particles. The corresponding simulation cases for different particle-fluid density ratios are denoted as Case 1, Case 2, Case 3, and Case 4. Regarding to the resolution needed for resolving the boundary layer on the particle surface, the thickness of the boundary layer near a particle can be roughly estimated by $\delta \approx d_p/\sqrt{\mathrm{Re}_p}$, where Re_p is the particle Reynolds number [37]. As can be seen in the following section, the largest mean Re_p in our simulation occurs in Case 4 which is 27.34, and this corresponds to $\delta = 1.5\delta x$ in the simulation. Thus the resolution should be adequate for most particles in the present study [33,37]. The particle volume fraction in the present particle-laden cases is fixed at 5% which is above the dilute limit, and hence the particle-particle interaction is important. The particles are released at around 40 eddy turnover times, and it takes another several eddy turnover times for the flow to reach the statistically stationary state.

A detailed flow statistics for the single-phase turbulence and particle-laden turbulence are given in Table I, including the Taylor microscale Reynolds number $\mathrm{Re}_\lambda = u'\lambda/\nu$, Kolmogorov length scale $\eta_k = (\nu^3/\varepsilon)^{1/4}$, Taylor microscale $\lambda = \sqrt{15\nu u'^2/\varepsilon}$, large eddy length scale $L_E = u'^3/\varepsilon$, Kolmogorov timescale $\tau_k = (\nu^3/\varepsilon)^{1/2}$, large eddy turnover time $\tau_E = L_E/u'$, skewness and flatness, where ν is the kinematic viscosity, u' is the r.m.s component fluctuation velocity and ε is the flow dissipation rate. It should be noted that the velocity inside the particles are assumed to take the form of rigid body motion. All the volume-averaged statistics are in lattice units and are averaged over the last 10 eddy turnover times within the statistically stationary state. The Stokes numbers defined by the Kolmogorov timescale (τ_k) of the single-phase flow are 4.39, 21.95, 87.79, and 439.96, respectively.

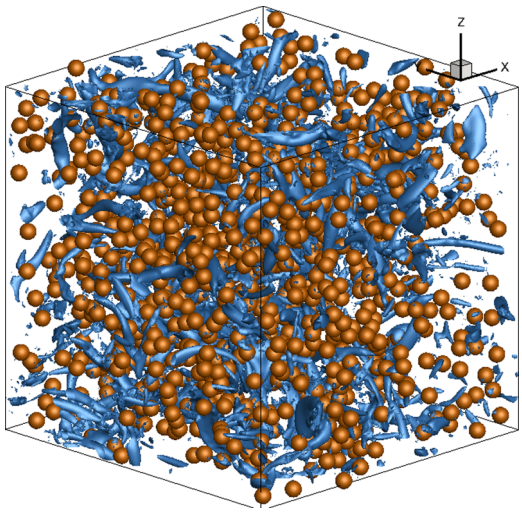

FIG. 2. Three-dimensional isosurface of vortical structures identified by Q criteria with $Q/\langle 2r_{ij}r_{ij}\rangle = 2.5$ for Case 1, and a small portion of the particles (30%) are shown to clearly see the vortical structures.

The particle-fluid density ratio has a significant influence on the turbulence intensity, and the turbulence intensity is decreasing with increasing particle-fluid density ratios as can be seen from (Re_λ) in Table I. Figure 2 shows the three-dimensional isosurface of vortical structures identified by Q criteria normalized by the average enstrophy ($\langle 2r_{ij}r_{ij}\rangle$) with $Q/\langle 2r_{ij}r_{ij}\rangle = 2.5$ for Case 1, where Q is given by $Q = -\frac{1}{2}(s_{ij}s_{ij} - r_{ij}r_{ij})$ with $s_{ij} = \frac{1}{2}(u_{i,j} + u_{j,i})$ and $r_{ij} = \frac{1}{2}(u_{i,j} - u_{j,i})$ the symmetric and the antisymmetric components of the fluid velocity gradient. Only 30 percent of the particles are shown in the figure for the sake of clarity, and the wormlike vorticity structures can be observed near the particles. As the turbulence attenuation is not the scope of this contribution, we will turn to the particle dynamics from now on.

A. Properties of individual particle motion

The Lagrangian statistics of the particles are obtained from averages of all particles in the system over about 10 eddy turnover times after the particle-laden turbulence reaches the statistically stationary state. Table II gives the standard deviation normalized by the Kolmogorov velocity scale, skewness and flatness of velocity and angular velocity. The particle velocity distribution is not sensitive to the particle-fluid density ratio, as all the skewness of three particle velocity components are close to 0 and the flatness are close to 3 for different cases which are consistent with the results from previous studies [19,20,25]. Hence the distribution of particle velocity is expected to be Gaussian. Figure 3 shows the distribution of three particle velocity components in Case 4. As shown in Fig. 3, the distribution of three particle velocity components are essentially Gaussian, figures are similar for the other three cases and have been omitted. Figure 4 shows the distribution

TABLE II. The standard deviation (σ), skewness (S), and flatness (F) of the components of particle velocity and angular velocity. The standard deviation of the velocity is normalized by the Kolmogorov velocity scale.

		Case1 $\rho^*=1$	Case2 $\rho^*=5$	Case3 $\rho^*=20$	Case4 $\rho^*=100$
	σ	4.534	3.270	2.192	1.643
$v_{p,x}$	S	−0.012	0.021	0.138	0.002
	F	2.739	2.725	2.772	3.051
	σ	4.370	3.247	2.223	1.630
$v_{p,y}$	S	−0.016	−0.050	0.089	0.005
	F	2.841	2.800	2.889	3.090
	σ	4.299	3.332	2.105	1.600
$v_{p,z}$	S	0.007	−0.084	−0.065	−0.006
	F	2.774	2.822	2.767	3.151
	σ	1.459E-3	8.801E-4	5.030E-4	2.208E-4
$\omega_{p,x}$	S	−0.056	−0.034	0.108	0.074
	F	4.994	4.076	3.795	3.439
	σ	1.447E-3	8.644E-4	4.909E-4	2.209E-4
$\omega_{p,y}$	S	−0.060	0.025	−0.036	−0.013
	F	4.568	4.117	3.563	3.487
	σ	1.464E-3	8.800E-4	4.890E-4	2.242E-4
$\omega_{p,z}$	S	0.038	0.038	−0.017	−0.050
	F	4.777	3.874	3.487	3.132

of three particle angular velocity components in Case 4. As can be seen from Table II, the distribution of angular velocity is slightly non-Gaussian with the flatness measured around 4 which is similar with the result of Zimmermann *et al.* [38], and a decrease of flatness with increasing inertia can be observed which indicates that the influence of fluid fluctuation becomes weaker when the particle inertia becomes large.

Figure 5 shows the distributions of three particle acceleration components for different cases. We only consider the acceleration contributed from the hydrodynamic force. The distribution exhibit long tails in Fig. 5 which indicate that

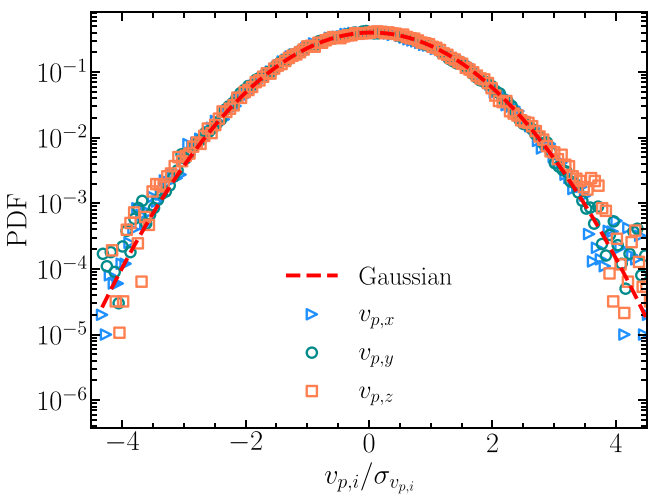

FIG. 3. The distribution of three velocity components for $\rho_p/\rho_f = 100$, the red dash line represents the Gaussian distribution.

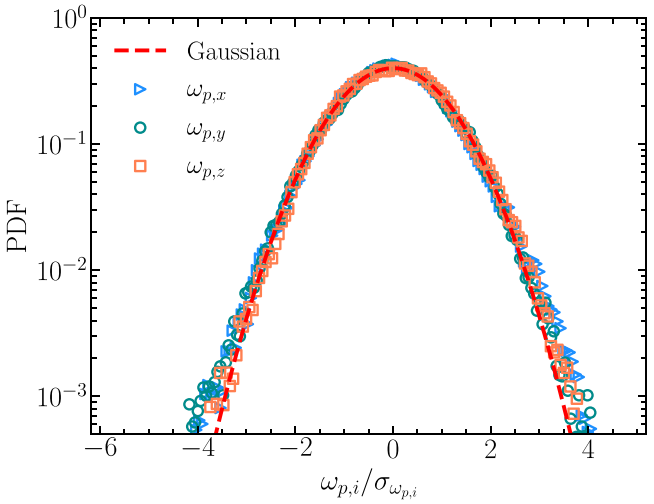

FIG. 4. The distribution of three angular velocity components for $\rho_p/\rho_f = 100$, the red dash line represents the Gaussian distribution.

they deviate from the Gaussian distribution. The particle acceleration is indeed highly intermittent, because the sweeping motion within a vortex may induce large acceleration of the particles as noted by Lee *et al.* [39] and Yeung *et al.* [40]. Mordant *et al.* [18] and Qureshi *et al.* [8,9] found the normalized distribution of particle acceleration is log-normal like with some empirical fitting parameters, and the empirical equation is given by

$$P(x) = \frac{e^{3s^2/2}}{4\sqrt{3}}\left[1 - \mathrm{erf}\left(\frac{\ln(|x/\sqrt{3}|) + 2s^2}{\sqrt{2}s}\right)\right], \qquad (3)$$

where s is the fitting parameter related to the shape of the probability density function (PDF). This form of the empirical equation, Eq. (3), was shown to be related to a log-normal distribution of variance s^2. The red dash line in Fig. 5 represents the empirical equation given by Eq. (3). It can be seen that the data of different cases can be roughly fitted to the empirical model proposed by Qureshi *et al.* [8,9], especially in the center region. The PDF of acceleration is similar with the work of Calzavarini *et al.* [11] with somewhat flatter tail. The flatness of acceleration for different cases can be seen in Table III, and it is found that the flatness decreases as particle-fluid density ratio increases. Two reasons might contribute to the decrease, the first is that the particles with small inertia can well respond to the intermittent turbulent flow, and the second might be the fact of particle collision as we do not exclude the colliding particles. Figure 6 shows the distribution of particle angular acceleration in z direction for different cases, the red dash line is the fitting curve using Eq. (3). We find the distribution can also be well described by the empirical function suggested by Qureshi *et al.* [8] with different fitting parameter. The fitting parameters are 0.79, 0.70 0.62, and 0.59, respectively, for Case 1, Case 2, Case 3, and Case 4. The decrease of s indicates a flatter peak in the figure. However, the normalized distribution in different cases are similar. The flatness of angular acceleration for particles in Case 4 is similar to the work of Zimmermann *et al.* [38] where a flatness of 7 was found for their large sphere particle.

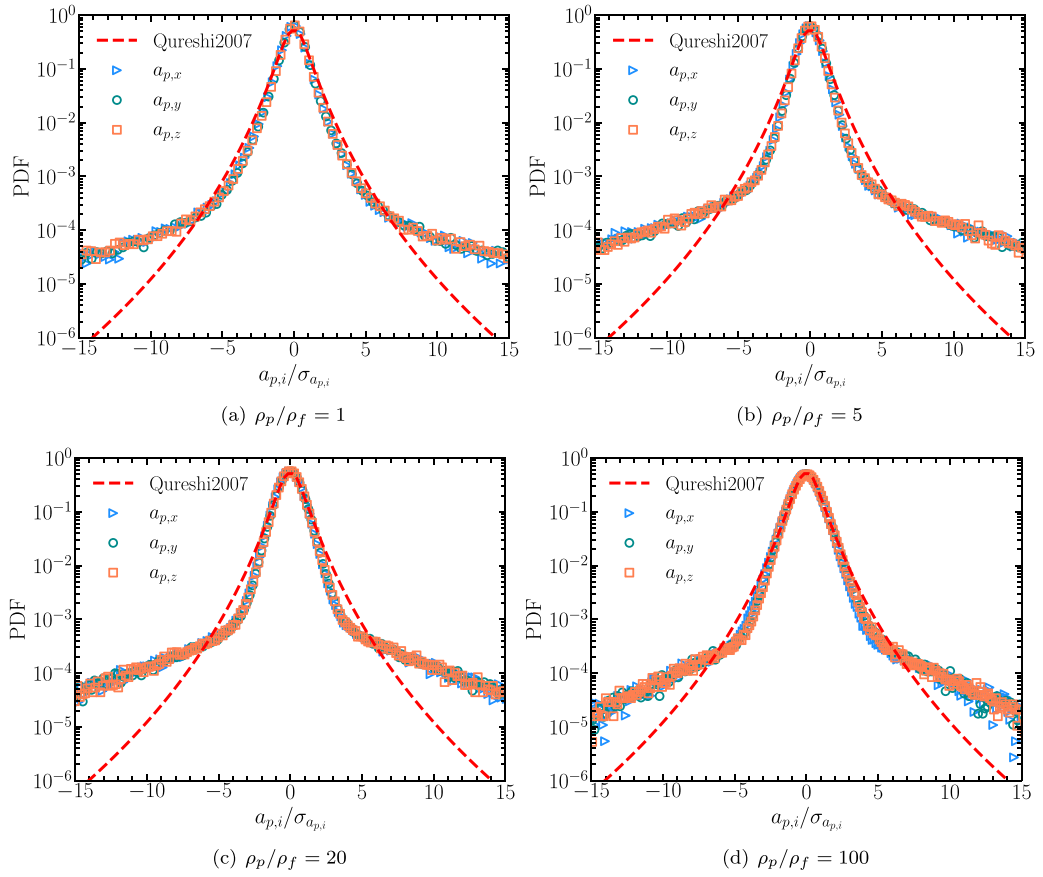

(a) $\rho_p/\rho_f = 1$ (b) $\rho_p/\rho_f = 5$

(c) $\rho_p/\rho_f = 20$ (d) $\rho_p/\rho_f = 100$

FIG. 5. The distributions of three particle acceleration components for different cases, the red dash line is the empirical equation proposed by Qureshi [8,9].

TABLE III. The standard deviation (σ), skewness (S), and flatness (F) of the components of particle acceleration and angular acceleration. The standard deviation of the acceleration is normalized by the Kolmogorov scale and Kolmogorov timescale.

		Case1 $\rho^* = 1$	Case2 $\rho^* = 5$	Case3 $\rho^* = 20$	Case4 $\rho^* = 100$
	σ	1.497	6.668E-1	1.981E-1	3.332E-2
$a_{p,x}$	S	−0.051	−0.022	0.003	−0.059
	F	225.70	146.92	83.99	28.86
	σ	1.488	6.766E-1	2.034E-1	3.365E-2
$a_{p,y}$	S	−0.147	0.025	0.062	0.070
	F	294.14	168.26	91.60	27.31
	σ	1.495	6.755E-1	2.027E-1	3.338E-2
$a_{p,z}$	S	−0.073	0.018	−0.016	0.049
	F	228.11	157.94	86.01	26.14
	σ	8.595E-6	2.372E-6	6.296E-7	1.139E-7
$\alpha_{p,x}$	S	0.025	0.042	−0.012	0.021
	F	23.98	24.49	12.83	7.48
	σ	8.590E-6	2.363E-6	6.192E-7	1.170E-7
$\alpha_{p,y}$	S	0.021	0.076	−0.014	−0.044
	F	19.59	23.57	13.45	7.36
	σ	8.462E-6	2.329E-6	6.225E-7	1.140E-7
$\alpha_{p,z}$	S	0.022	0.072	−0.040	−0.010
	F	19.94	20.28	14.51	7.27

In addition to the statistics mentioned above, how would finite-size particles follow the local fluid motion is always of scientific interest. The particle-fluid relative velocity is one of quantitative descriptions which measure the velocity

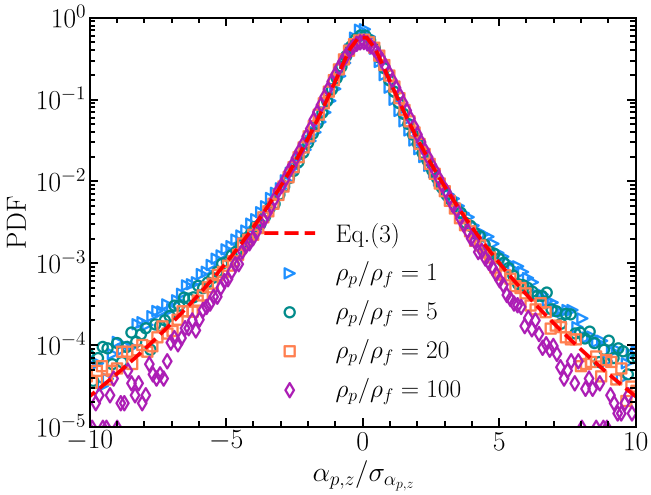

FIG. 6. The distribution of angular acceleration in z direction for different cases, the red dash line is the fitting curve in Eq. (3), the fitting parameter is the average over different cases which corresponds to 0.69.

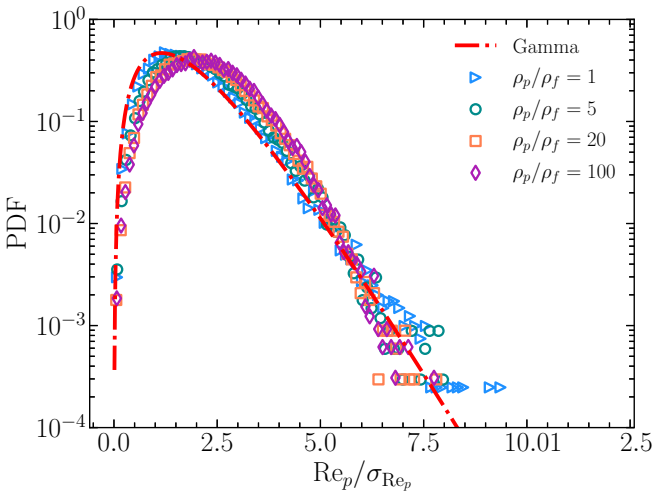

FIG. 7. PDF of particle Reynolds number for different cases, the red dashed line is the gamma distribution suggested by Uhlmann *et al.* [25] for particles with particle-fluid density ratio 1.5.

difference between two phases, and a zero relative velocity is expected for tracers. As in particle resolved simulations, the local fluid is occupied by the finite-size particles and the definition of local fluid velocity in particle center is controversial [41,42]. Here we define the local fluid velocity with respect to the ith particle by averaging over a sphere shell between the particle surface and a sphere surface with diameter D_s centered at the center of the particle. The averaging diameter is set to $D_s = 3d_p$ in this paper, where d_p is particle diameter. The distribution of particle Reynolds number based on the particle-fluid relative velocity can be obtained when the local fluid velocity seen by the particles are obtained, the instantaneous particle Reynolds number is defined as $\mathrm{Re}_p^{(i)}(t) = |v_p^{(i)} - u_f^{(i)}|d_p/\nu$. Here we investigate the influence of particle-fluid density ratio on the distribution of particle Reynolds number. Figure 7 shows the distribution of Re_p for different cases, it is seen that the mean of the normalized distribution of Re_p shifts to the right with increasing particle-fluid density ratio as the particles fail to follow local fluid motion with increasing density and the velocity difference becomes larger. This can also be observed from Table IV, the mean value of particle Reynolds number increases with particle-fluid density ratio. Uhlmann *et al.* [25] found that probability density function (PDF) of the the particle Reynolds number Re_p normalized by the standard deviation is close to a gamma distribution with shape parameter $k = 3$ in their simulations. As shown in Fig. 7 for neutrally buoyant particles of density ratio 1 in Case 1 which is close to the particle-fluid density ratio 1.5 in their work, the match is good with a flatness of 5.13 where the flatness is 5 for gamma distribution. Another indicator for the ability of particles to follow the local fluid motion is the alignment angle between (θ_{align}) particle and local fluid velocity vector as in Fig. 8(a), and the alignment angle is defined as the solid angle. The PDFs of the θ_{align} for different cases are show in Fig. 8(b). As can be seen from Fig. 8(b), the neutrally buoyant particles follow the local fluid velocity well as a sharp peak locates at $\theta_{\mathrm{align}} \approx 0$ can be seen, and the ability to follow local fluid motion becomes weaker as the particle-fluid density ratio increases. For particles in Case 2, the distribution becomes wider near $\theta_{\mathrm{align}} \approx 0$, indicating a weaker ability to follow local fluid motion, but the alignment is still good as a relative sharp peak at $\theta_{\mathrm{align}} \approx 0$ can also be observed. The distribution is almost uniform for heavy particles in Case 4, indicating a very weak correlation between the direction of particle velocity and local fluid velocity which results from the cross-trajectory effect.

TABLE IV. Mean value and standard deviation of the particle Reynolds number (Re_p) in different cases.

	Case 1 $\rho^* = 1$	Case 2 $\rho^* = 5$	Case 3 $\rho^* = 20$	Case 4 $\rho^* = 100$
Mean	13.10	18.00	23.97	27.34
σ_{Re_p}	6.92	8.68	10.83	11.86

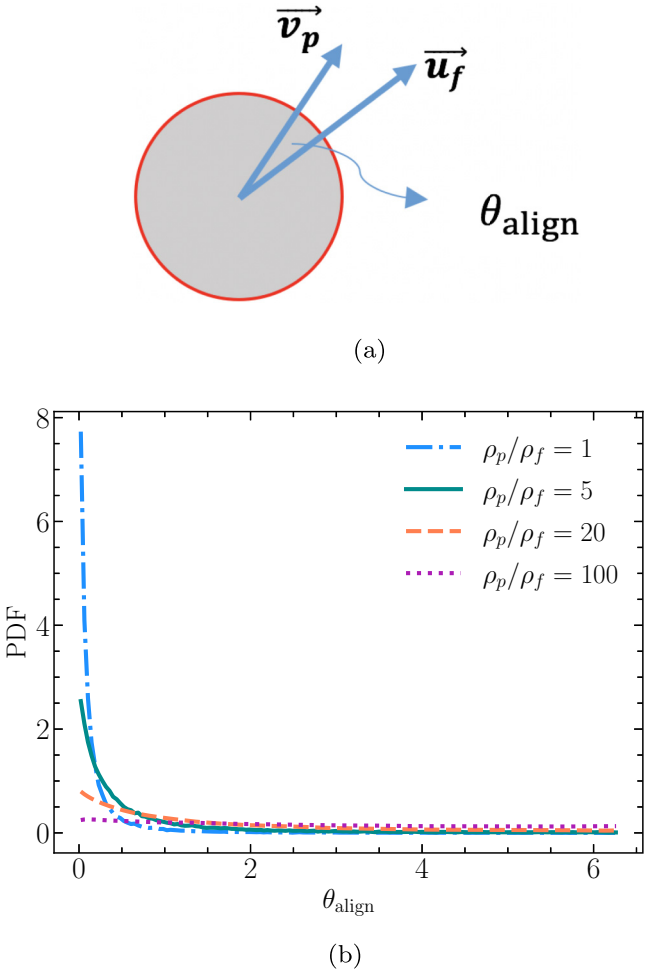

FIG. 8. (a) Sketch of the alignment angle (θ_{align}) between particle and fluid velocity and (b) PDF of the alignment angle (θ_{align}) between particle and fluid velocity. As the particle-fluid density ratio increases, the ability of particles to follow the local fluid motion becomes weaker as the peak value becomes smaller and the distribution becomes wider, and the heavy particles exhibit an almost uniform distribution.

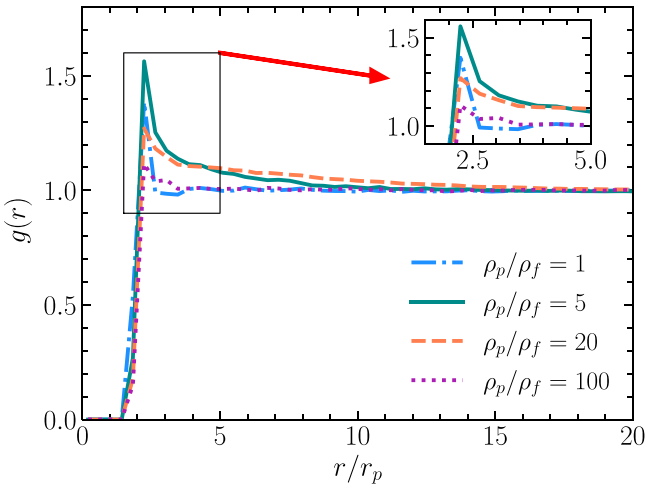

FIG. 9. Radial distribution function for different cases, the x axis is the distance from particle center normalized by particle radius. The inset shows a zoom of the region near the peak.

B. Particle preferential concentration

Inertial particles are known to form local high concentration regions rather than randomly distributed in the turbulence because the inertia of particles prevent them from following the fluid motion. From the analysis above, the finite-size particles with different particle-fluid density ratio respond differently to the flow and thus show different ability to follow the local fluid motion, which will in fact affect their spatial position and distribution in the carrier flow. For particle spatial distribution, the radial distribution function (RDF) is usually employed to characterize the spatial distribution of particles, which is defined as $g(r_i) = \frac{N_i/V_i}{N/V}$, where N_i is the number of particle pairs whose distance between two centers is within an interval $(r_i - \delta_r, r_i + \delta_r)$, where r_i is the center of ith detection shell, $2\delta_r$ is the width of the detection shell, V_i is the shell volume, and N is the number of particle pairs in the whole computational domain with the control volume V. The RDF represents the relative probability of finding particle pairs with center distance r, and a RDF larger than one indicates that some particle aggregates may exist in the system. Figure 9 shows the RDF for all four test cases, from which the peaks of the RDF appearing close to $r = 2r_p$ can be observed for different cases, indicating that the aggregates formed during the collision process mainly containing two primary particles. The relative small maximum values of the RDF reveal that the preferential concentration in present simulations is weak which can also be noticed from Voronoï diagram in the next paragraph, especially for Case 4 where the peak value is 1.1. Besides the largest peak value near $r/r_p = 2$ for the RDF of particles in Case 2, a long tail in the curvature with $g(r) > 1$ can be seen, indicating clusters composed of more than two particles form in Case 2. By comparing RDF of Case 1 and Case 3, although the peak value of $g(r)$ in Case 1 is slightly larger than that in Case 3, a long tail with $g(r) > 1$ in Case 3 can be observed, revealing that clusters also form in Case 3. Even larger values of $g(r)$ in Case 3 for $r/r_p > 4$ is noticed comparing with Case 2, and this might indicate the preferential concentration is also strong in Case 3. As can be seen from the next paragraph, the PDF of the normalized Voronoï cells are similar in Case 2 and Case 3. The reason is that particles in Case 1 follow the fluid motion well and particles in Case 4 fails to follow the fluid motion, which all will lead to the more uniform spatial distribution of particles. Intermediate density ratio particles in Case 2 and Case 3 would interact more intensely with the local fluid vortical structures at the scale of particle diameter and result in a more remarkable preferential concentration. Figures 10(a), 10(b), 10(c) and 10(d) show the snapshots of the vorticity contour of the flow field for different cases. High vorticity regions near particle surfaces can be observed from the figures for different cases especially for Case4, and the vorticity near the particle surfaces becomes higher with the increasing particle-fluid density ratio which indicates the dissipation becomes relatively larger. It might be the reason for the decrease of turbulence intensity which is observed in Table I. The interaction between particles and local fluid vortical structures needs further investigation and will not be discussed here.

The Voronoï diagram is another well-known method to analyze the spatial distribution of the dispersed particles, and it provides a detailed information where particles accumulate while RDF only gives the global information. For the three-dimension distribution of particles, the volumes of the Voronoï cells are inversely proportional to the local concentration of particles, the local high particle concentration regions are represented by the regions with the existence of small Voronoï cells. Snapshots of the 2D slice of Voronoï cells for different cases can be seen from Figs. 10(b), 10(e), 10(h), and 10(k), particles intersect with the plane are also shown on the slice. As can be seen from the Fig. 10(k), the particles in Case 4 exhibit the most uniform spatial distribution among different cases as the sizes of Voronoï cells are more uniform compared to Figs. 10(b), 10(e), and 10(h) and regions with small Voronoï cell sizes can hardly be found. Although some regions with small Voronoï cells exist for particles in Case 1 as shown in Fig. 10(b), a larger probability to see regions with small and large cells can be observed in Figs. 10(e) and 10(h) which indicates the nonuniformity of particle spatial distribution is stronger in Case 2 and Case 3. The nonuniformity of the particle spatial distribution can be quantitatively analyzed form the distribution of the Voronoï cell volumes. Figure 11 shows the distribution of the logarithm of Voronoï cell volumes, and the data is also centered and normalized. The red dash line is a Gaussian distribution for comparison, the distribution is of excellent agreement within the interval $[-3\sigma_{\log(V)}, 3\sigma_{\log(V)}]$, where $\sigma_{\log(V)}$ is the standard deviation. Our simulations confirm that the distribution of Voronoï cell volumes is well described by the log-normal distribution as noted by Monchaux *et al.* [23]. However, although the log-normal distribution predicts the distribution of Voronoï cell volumes well, the degree of preferential concentration cannot be obtained by comparing with such log-normal distribution. To compare the difference between the distribution of different cases, the normalized distributions of Voronoï cell volumes rather than the logarithm of Voronoï cell volumes are shown in Fig. 12, it can be seen that the distribution for Case 1 and Case 4 and the distribution for Case 2 and Case 3 almost

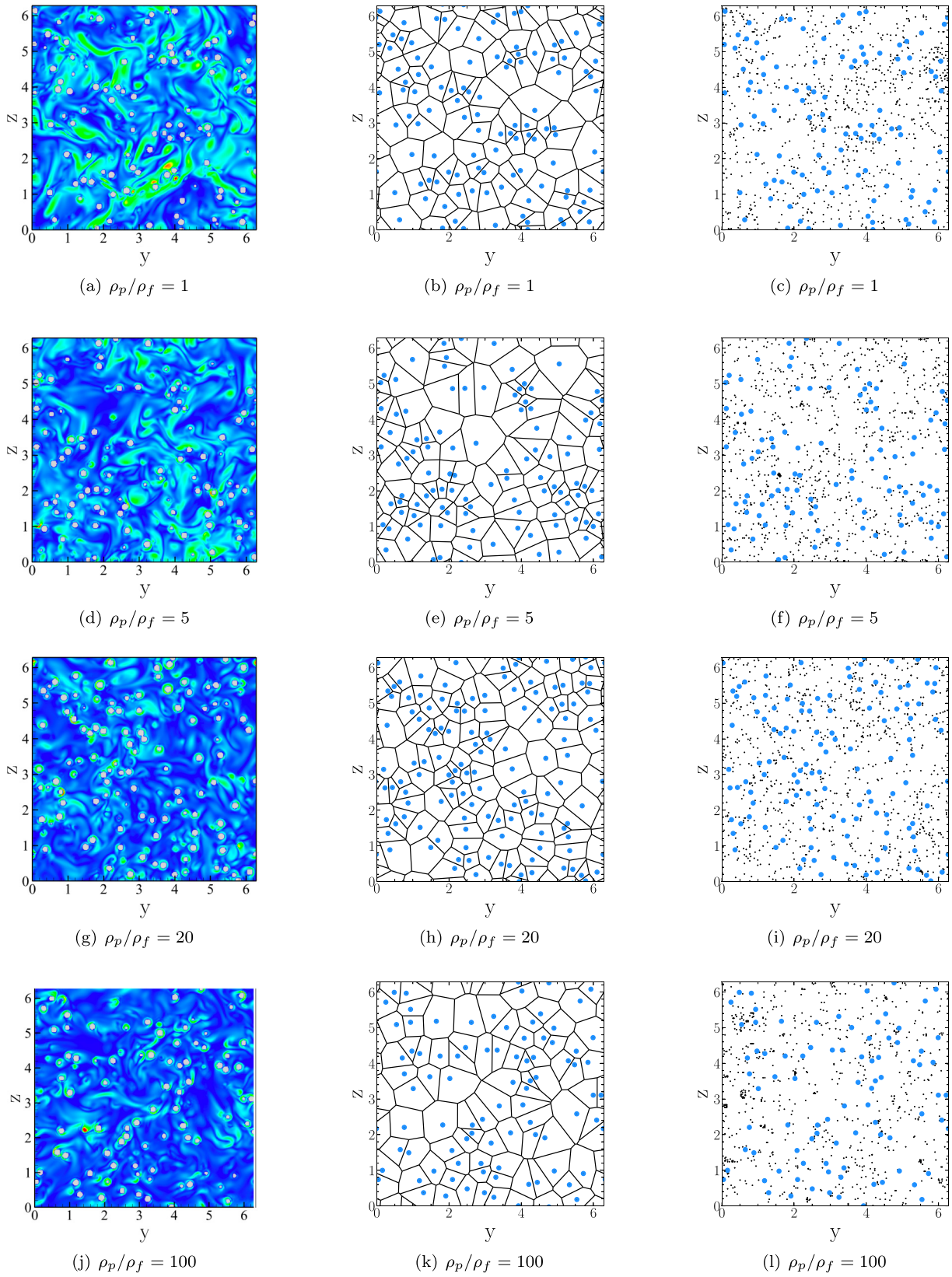

(a) $\rho_p/\rho_f = 1$ (b) $\rho_p/\rho_f = 1$ (c) $\rho_p/\rho_f = 1$

(d) $\rho_p/\rho_f = 5$ (e) $\rho_p/\rho_f = 5$ (f) $\rho_p/\rho_f = 5$

(g) $\rho_p/\rho_f = 20$ (h) $\rho_p/\rho_f = 20$ (i) $\rho_p/\rho_f = 20$

(j) $\rho_p/\rho_f = 100$ (k) $\rho_p/\rho_f = 100$ (l) $\rho_p/\rho_f = 100$

FIG. 10. 2D visualization for different cases on a slice at $x = 127.5$, figures for the same case are at the same time step. Panels (a), (d), (g), (j) are the vorticity fields, the color represents the magnitude of vorticity. High-vorticity regions near particle surfaces in all cases especially in Case 4 can be observed. Panels (b), (e), (h), (k) are the Voronoï diagrams, the particles insect with the plane are also shown and are represented by the skyblue spheres. Panels (c), (f), (i), (l) show spatial locations of particles and sticky points, the black dots are sticky points and the skyblue spheres are particles.

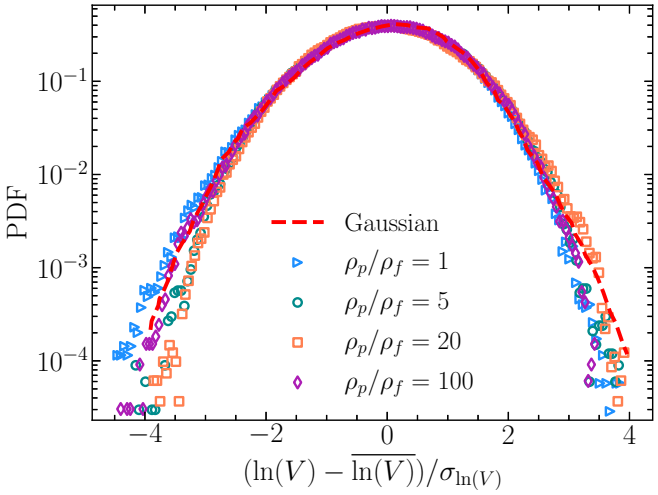

FIG. 11. Centered and normalized PDF of the logarithm of Voronoï cell volumes, the red dash is a Gaussian distribution for comparison.

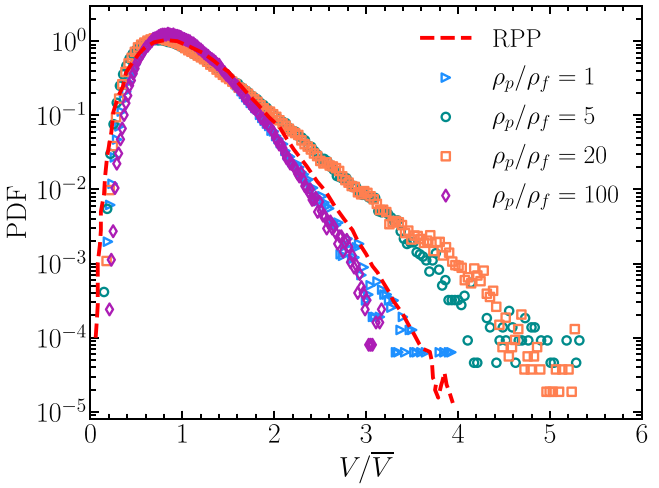

FIG. 12. PDF of the normalized Voronoï cells, RPP represents results from random Poisson process.

collapses, indicating the levels of preferential concentration might be similar for the two groups. For Case 2 and Case 3, an increasing probability to see large and small Voronoï cells can be observed which reveals a more pronounced preferential concentration. Point particles distributed randomly and uncorrelatedly are usually considered drawn from the random Poisson process (RPP), and the distribution of the corresponding Voronoï cell volumes is a gamma distribution with parameters proposed by Ferenc and Neda [43]. We thus compare the PDF of Voronoï cell volumes normalized by the average cell volume ($V_{\text{vor}} = V/\langle V \rangle$) from our simulations with that for RPP in Fig. 12. The distributions for Case 1 and Case 4 are close to the γ distribution for RPP but are slightly narrower which indicates the preferential concentration is weak. The distribution for Case 2 exhibits more large and small Voronoï cells compared to RPP which indicates the preferential concentration is stronger. Next we analyze the standard deviation of the Voronoï cell volumes which is approximately 0.42 for a 3D Random Poisson Process system as noted by Ferenc *et al.* [43]. A standard deviation higher than 0.42 indicates the higher possibility of local high and low particle concentration, and a value below the reference value indicate that the particles tend to distribute more randomly and the preferential effect is weak. They are 0.37, 0.48, 0.47, and 0.35, respectively, for Case 1, Case 2, Case 3, and Case 4 in our simulations, which is consistent with the shape of the PDF in Fig. 12 for different cases.

To further investigate the mechanism of the spatial nonuniform distribution of particles, we consider the sweep-stick mechanism proposed by Goto and Vassilicos [26]. It has been reported that the preferential concentration of particles is strongly related to the fluid acceleration for small particles. The particles potentially accumulate at the stagnation points of fluid acceleration to which we refer as 'sticky point'. Whether the sweep-stick mechanism holds for finite-size particles with different densities is yet still a question to be explored. The sweep-stick mechanism assumes the Stokes drag limit where the equation for motion of the particles is

$$\frac{d\boldsymbol{v_p}}{dt} = -\frac{1}{\tau_p}(\boldsymbol{v_P} - \boldsymbol{u_f}); \tag{4}$$

the following approximation can be made if the stokes number is small and the particles are considered as tracers:

$$\boldsymbol{v_p} - \boldsymbol{u_f} \approx -\tau_p \boldsymbol{a_f}. \tag{5}$$

The clusters of particles will form while the divergence of particle velocity is less than 0 ($\boldsymbol{\nabla} \cdot \boldsymbol{v_p} < 0$), which corresponds to the regions where the divergence of fluid acceleration is larger than 0 ($\boldsymbol{\nabla} \cdot \boldsymbol{a_f} > 0$). Specifically, the convergence mainly occurs along the direction parallel to the eigenvector corresponding to the largest positive eigenvalue of the symmetric part of the fluid acceleration gradient tensor ($\boldsymbol{\nabla a_f} + (\boldsymbol{\nabla a_f})^T$). Thus, the sticky points obeying the above convergence can be expressed by the following criterion:

$$\boldsymbol{e_1} \cdot \boldsymbol{a_f} = 0, \quad \lambda_1 > 0, \tag{6}$$

where λ_1 is the largest positive eigenvalue of the symmetric part of the fluid acceleration gradient tensor and $\boldsymbol{e_1}$ is the corresponding eigenvector. In practice, the fluid points are considered as sticky point where the dot product is smaller than a threshold value ($\sigma_{\text{threshold}} = \gamma_{\text{sp}}\sigma_{\text{sp}}$), where σ_{sp} is the standard deviation of $\boldsymbol{e_1} \cdot \boldsymbol{a_f}$.

As noted in Goto and Vassilicos [26], the largest eigenvalues of symmetric part of the fluid acceleration (λ_1) is of the order of τ_η^{-2}. Figure 13 shows the distribution of λ_1 normalized by the Kolmogorov timescale in Case 4, the figures are similar for the other three cases. The result from our simulations show that λ_1 is indeed of the order of τ_η^{-2}. The positive values of λ_1 are of concerns as the sticky points are defined as $\lambda_1 > 0$ and a larger amount of positive λ_1 can be observed actually. Then we investigate the spatial correlation between particle position and sticky points. Figures 10(c), 10(f), 10(i), and 10(l) show the instantaneous visualizations of the location of sticky points and particles for different cases, and the visualizations show slices of thickness equal to the particle diameter along the direction normal to the

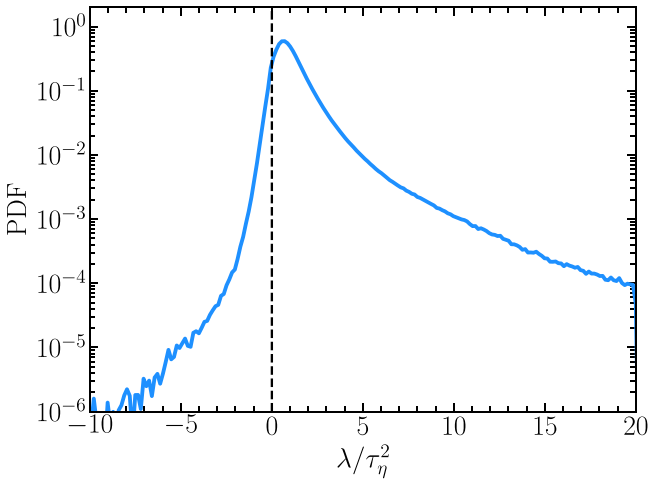

FIG. 13. PDF of the largest eigenvalue λ_1 of symmetric part of the fluid acceleration gradient, $\rho_p/\rho_f = 100$.

plane. The black dots are the sticky points detected using above criterion and the skyblue spheres are the particles. It can be observed that the spatial distribution of sticky points is inhomogeneous distributed with dense regions, dilute regions and voids. It can also be observed that there are many sticky points located around the particle surfaces, indicating a correlation between the location of particles and sticky points do exist. To quantitatively investigate the correlation between the location of particles and sticky points, we calculate the particle conditional radial distribution function which measures the possibility to find sticky points within a given distance interval away from the particle surfaces. The conditional RDF is defined as $g_{\mathrm{con}}(r_i) = \frac{N_{i,\mathrm{sp}}/V_{i,\mathrm{sp}}}{N_{\mathrm{sp}}/V_{\mathrm{sp}}}$, where $N_{i,\mathrm{sp}}$ is the number of sticky points with center distance from particle within an interval $(r_i - \delta_r, r_i + \delta_r)$, where r_i is the center of ith detection shell, $2\delta_r$ is the width of the detection shell, $V_{i,\mathrm{sp}}$ is the shell volume, and N_{sp} is the number of particle-sticky-point pairs in the whole computational domain with the control volume V_{sp}. Figure 14 shows the conditional RDF averaged over all particles in the system and different times, and the x axis is the distance away from the particle surface normalized by particle radius. As can be observed from Fig. 14, the particle conditional RDF exhibits a peak at 0 or close to 0 which corresponds to the particle surface for all cases, indicating the particle location is correlated to the sticky points. Although the peaks exist for all cases, some differences can be observed. By comparing Figs. 14(a) and 14(b), a smaller peak value for Case 1 can be observed which reveal the preferential concentration in Case1 is weaker than Case 2, and this is consistent with the result of RDF in Fig. 9. The maximum amplitude of the particle conditional RDF is approximately 1.2 times the global probability, and this relatively small value

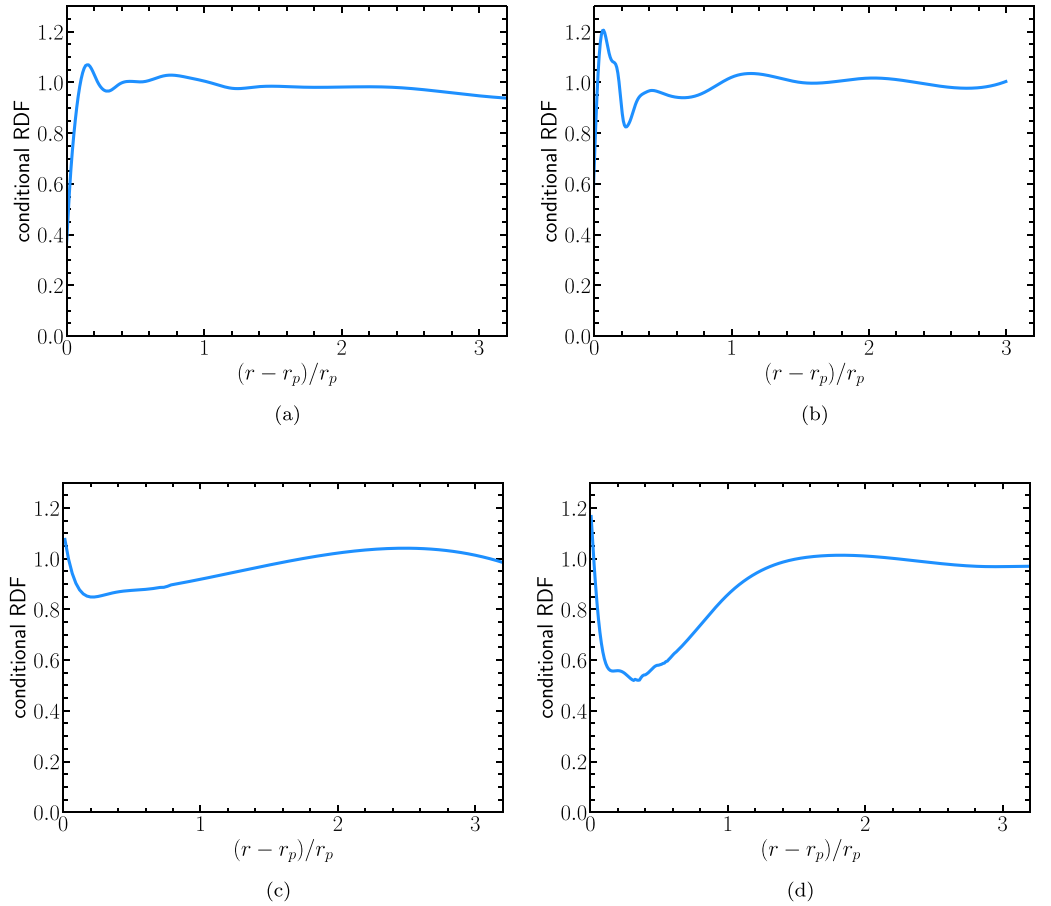

FIG. 14. Particle conditional RDF as a function of the distance from particle surface normalized by particle radius for different cases. (a) $\rho_p/\rho_f = 1$, (b) $\rho_p/\rho_f = 5$, (c) $\rho_p/\rho_f = 20$, and (d) $\rho_p/\rho_f = 100$.

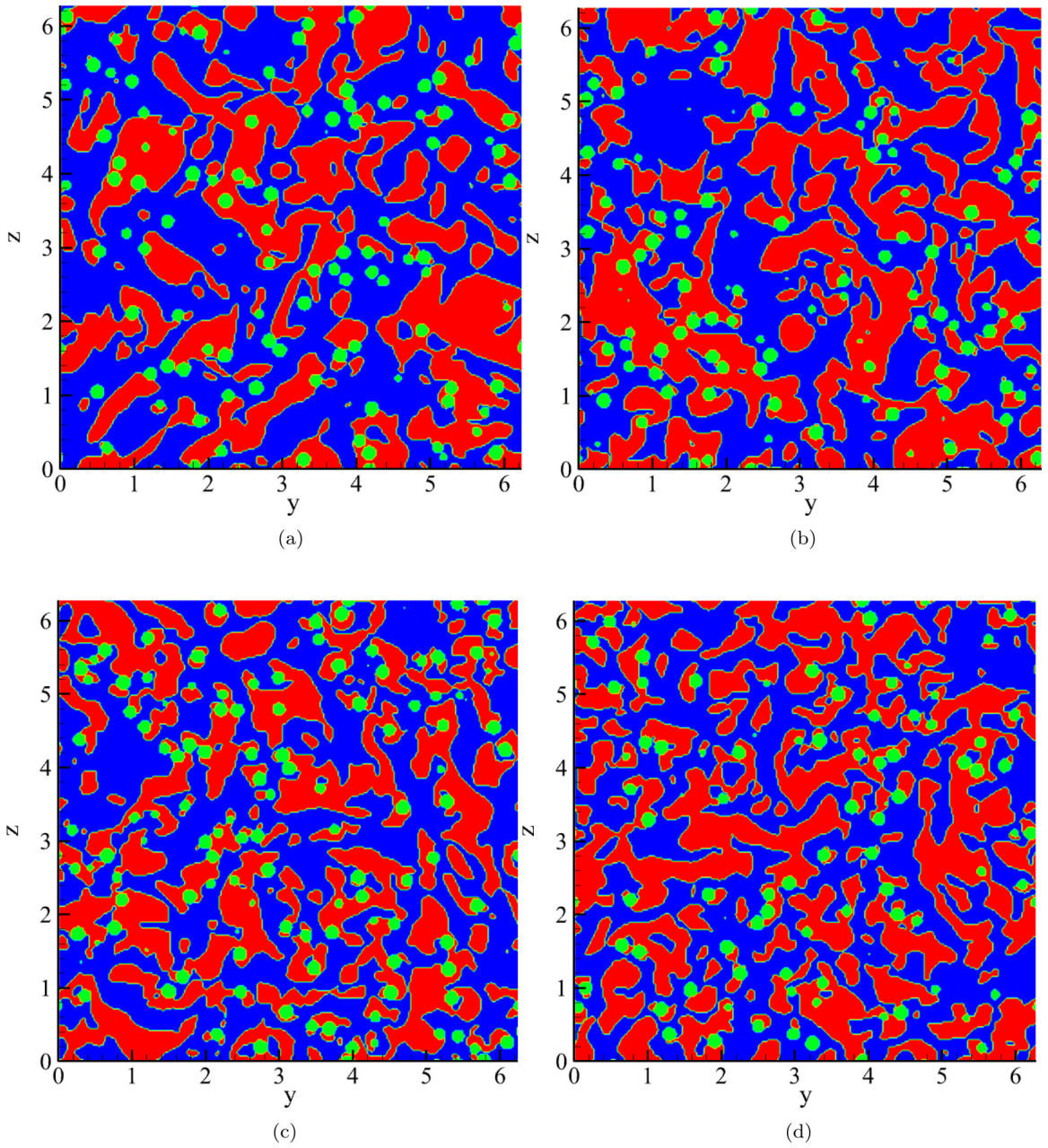

FIG. 15. Regions of different signs of the coarse-grained Q using the Q criterion, the red color represents the region where $\widetilde{S} : \widetilde{S} - \widetilde{R} : \widetilde{R} < 0$, the blue color represents the region where $\widetilde{S} : \widetilde{S} - \widetilde{R} : \widetilde{R} > 0$, and the green color represents the solid particles. (a) $\rho_p/\rho_f = 1$, (b) $\rho_p/\rho_f = 5$, (c) $\rho_p/\rho_f = 20$, and (d) $\rho_p/\rho_f = 100$.

corresponds to the overall weak preferential concentration in this study. From Figs. 14(c) and 14(d), a reduction of the conditional RDF can be observed, and this imply that the sticky mechanism might fail to predict the particle location.

These finding can be qualitatively explained by the drift mechanism for particle clustering proposed by Bragg *et al.* [28,29]. First, they found that with the increase of St, the significance of sticky points for the particle motion becomes weaker, and the effect becomes very weak when St = 30 in their work [28]. Second, they demonstrated that the sticky points tend to exist in regions where $\widetilde{S} : \widetilde{S} - \widetilde{R} : \widetilde{R} > 0$, where $\widetilde{S}$ and $\widetilde{R}$ are the coarse-grained strain-rate and rotation-rate tensor averaged along the inertial particle trajectory. Thirdly, they related the particle clustering mechanism to the scale-dependent Stokes number $\mathrm{St}_r = \tau_p/\tau_r$, where τ_r is the eddy turnover time of length scale r defined as $\tau_r = r^{2/3}\varepsilon^{-1/3}$. They found that particles tend to accumulate in the high local coarse-grained strain-rate region due to centrifuge mechanism when $\mathrm{St}_r \ll 1$ and the nonlocal, path-history symmetry-breaking mechanism contributes to the clustering when $\mathrm{St}_r \gtrsim 1$. Figure 15 shows the regions of different signs of coarse-grained Q which is obtained using the Q criterion, and the filtering scale is selected as the particle diameter d_p. We can see that the particles in Case 2, Case 3, and Case 4 tend to accumulate in the rotation dominant region where $\widetilde{S} : \widetilde{S} - \widetilde{R} : \widetilde{R} < 0$ (region with red color), and

this may lead to the reduction of conditional RDF of sticky points. The particles in Case 1 are more likely to appear in the region where $\widetilde{S} : \widetilde{S} - \widetilde{R} : \widetilde{R} > 0$. While the length scale is selected as the particle diameter (d_P), the corresponding St_r are 1.02, 5.15, 20.60, and 103.22 for different cases. We find that the particle clustering in Case 1 can also be attributed to the centrifuge mechanism, and the particle clustering of other cases can be attributed to the nonlocal, path-history symmetry-breaking mechanism.

IV. SUMMARY AND DISCUSSION

The interface-resolved direct numerical simulations based on lattice Boltzmann method incorporating interpolated bounce-back method are performed to investigate the influence of particle-fluid density ratio on the dynamics of finite-size particles in homogeneous isotropic turbulent flows. At the particle release time, the Taylor microscale Reynolds number is 76, and particle diameter is 8.9 times that of the smallest scale in turbulence (Kolmogorov scale). Gravity is neglected in the simulation to avoid the additional energy injection. Four different particle-fluid density ratios are simulated, and the volume fraction of the solid phase is fixed at 5%.

First, particle Lagrangian statistics such as velocity and angular velocity are studied for different cases, the statistics are obtained through the average over sufficient long time interval for all the particles in the computational domain after the flow reaches the statistical stationary state. Compared with the velocity and angular velocity, the particle acceleration and angular acceleration are more sensitive to the particle-fluid density ratio. The heavy particles are less influenced by the intermittency of the carrier flow. The acceleration and angular acceleration are intermittent quantities as they deviate from the Gaussian distribution greatly. The angular acceleration is also found to be well described by the Log-Normal like distribution proposed by Qureshi *et al.* [8,9]. Then the particle Reynolds number and the alignment angle between particle velocity and local velocity are studied to check how the particles follow the local fluid motion. It is found that, with the increase of particle-fluid density ratio, the velocity difference between two phases becomes larger, the mean value of the particle Reynolds number becomes larger, and the ability of particles to follow the local fluid motion becomes weaker.

Next, as the different correspondence of particles to the flow will affect the particle spatial distribution, the difference in spatial distributions between different cases are then analyzed. RDF and Voronoï tessellation are used to investigate the spatial distribution of particles, and both analysis show that the preferential concentration is most profound for intermediate density particles and the particle-fluid density ratio is important for the preferential concentration of particles. The neutrally buoyant particles follow the fluid well and the heavy particles can hardly follow the local fluid, both reasons will lead to a more uniform spatial distribution of particles. The vortical structures may play an important role which lead to the non uniform spatial distribution of finite-size particles. From Voronoï tessellation, the distribution of Voronoï cells is better described by the log-normal distribution which is in good agreement, but information of the degree of preferential concentration is missed from the log-normal distribution. Furthermore, we check the correlation between the position of sticky points and particles, although we do find a higher probability of particles being located near the sticky points in different cases, the significance of stagnation points for particle motion is very small for particles with large particle-fluid density ratio. With respect to the particle accumulation, we found that the drift mechanism can qualitatively explain the clustering of particles. For a small St_r in Case 1, the particle locates in the high coarse-grained strain-rate regions due to centrifuge effect. For larger St_r, the nonlocal, path-history symmetry-breaking mechanism is important for the clustering of particles.

In summary, the particle-fluid density ratio influences the particle response to the carrier flow and thus result in the different spatial distribution of particles. The particle-fluid density ratio is a key parameter strongly correlated to the preferential concentration of particles, and thus is important in the prediction of the formation of particle clusters. However, the particle-fluid density ratio region which lead to the strongest preferential concentration remains to be explored. Besides, whether the turbulence intensity and the volume fraction are import factors for particle acceleration and preferential concentration requires further study.

ACKNOWLEDGMENTS

We acknowledge the support from Natural Science Foundation of China with Grants No. 11732010, No. 12072185, No. 11988102, and No. 91852205.

[1] A. J. Prata and A. Tupper, Aviation hazards from volcanoes: The state of the science, Nat. Hazards **51**, 239 (2009).

[2] W. W. Grabowski and L.-P. Wang, Growth of cloud droplets in a turbulent environment, Annu. Rev. Fluid Mech. **45**, 293 (2013).

[3] M. R. Maxey and J. J. Riley, Equation of motion for a small rigid sphere in a nonuniform flow, Phys. Fluids. **26**, 883 (1983).

[4] A. D. Bragg, P. J. Ireland, and L. R. Collins, On the relationship between the nonlocal clustering mechanism and preferential concentration, J. Fluid Mech. **780**, 327 (2015).

[5] S. Elghobashi and G. Truesdell, On the two-way interaction between homogeneous turbulence and dispersed solid particles. I. Turbulence modification, Phys. Fluids. A **5**, 1790 (1993).

[6] A. Prosperetti, Life and death by boundary conditions, J. Fluid Mech. **768**, 1 (2015).

[7] S. Tenneti and S. Subramaniam, Particle-resolved direct numerical simulation for gas-solid flow model development, Annu. Rev. Fluid Mech. **46**, 199 (2014).

[8] N. M. Qureshi, M. Bourgoin, C. Baudet, A. Cartellier, and Y. Gagne, Turbulent Transport of Material Particles: An

Experimental Study of Finite Size Effects, Phys. Rev. Lett. **99**, 184502 (2007).

[9] N. M. Qureshi, U. Arrieta, C. Baudet, A. Cartellier, Y. Gagne, and M. Bourgoin, Acceleration statistics of inertial particles in turbulent flow, Eur. Phys. J. B **66**, 531 (2008).

[10] L. Fiabane, R. Zimmermann, R. Volk, J.-F. Pinton, and M. Bourgoin, Clustering of finite-size particles in turbulence, Phys. Rev. E **86**, 035301(R) (2012).

[11] E. Calzavarini, R. Volk, M. Bourgoin, E. Lévêque, J.-F. Pinton, and F. Toschi, Acceleration statistics of finite-sized particles in turbulent flow: The role of faxén forces, J. Fluid Mech. **630**, 179 (2009).

[12] M. Maxey, Simulation methods for particulate flows and concentrated suspensions, Annu. Rev. Fluid Mech. **49**, 171 (2017).

[13] C. S. Peskin, The immersed boundary method, Acta Numer. **11**, 479 (2002).

[14] A. J. C. Ladd and R. Verberg, Lattice-Boltzmann simulations of particle-fluid suspensions, J. Stat. Phys. **104**, 1191 (2001).

[15] M. Bouzidi, M. Firdaouss, and P. Lallemand, Momentum transfer of a Boltzmann-lattice fluid with boundaries, Phys. Fluids **13**, 3452 (2001).

[16] W. Zhao and W.-A. Yong, Single-node second-order boundary schemes for the lattice Boltzmann method, J. Comput. Phys. **329**, 1 (2017).

[17] C. Peng, Y. Teng, B. Hwang, Z. Guo, and L.-P. Wang, Implementation issues and benchmarking of lattice Boltzmann method for moving rigid particle simulations in a viscous flow, Comput. Maths Applics. **72**, 349 (2015).

[18] N. Mordant, A. M. Crawford, and E. Bodenschatz, Three-Dimensional Structure of the Lagrangian Acceleration in Turbulent Flows, Phys. Rev. Lett. **93**, 214501 (2004).

[19] K. Yeo, S. Dong, E. Climent, and M. R. Maxey, Modulation of homogeneous turbulence seeded with finite size bubbles or particles, Intl J. Multiphase Flow **36**, 221 (2010).

[20] H. Homann and J. BEC, Finite-size effects in the dynamics of neutrally buoyant particles in turbulent flow, J. Fluid Mech. **651**, 81 (2010).

[21] S. Balachandar and J. K. Eaton, Turbulent dispersed multiphase flow, Annu. Rev. Fluid Mech. **42**, 111 (2010).

[22] L.-P. Wang and M. R. Maxey, Settling velocity and concentration distribution of heavy particles in homogeneous isotropic turbulence, J. Fluid Mech. **256**, 27 (1993).

[23] R. Monchaux, M. Bourgoin, and A. Cartellier, Preferential concentration of heavy particles: A Voronoï analysis, Phys. Fluids **22**, 103304 (2010).

[24] R. Monchaux, M. Bourgoin, and A. Cartellier, Analyzing preferential concentration and clustering of inertial particles in turbulence, Intl J. Multiphase Flow **40**, 1 (2012).

[25] M. Uhlmann and A. Chouippe, Clustering and preferential concentration of finite-size particles in forced homogeneous-isotropic turbulence, J. Fluid Mech. **812**, 991 (2016).

[26] S. Goto and J. C. Vassilicos, Sweep-Stick Mechanism of Heavy Particle Clustering in Fluid Turbulence, Phys. Rev. Lett. **100**, 054503 (2008).

[27] G. Wang, D. Wan, C. Peng, K. Liu, and L. P. Wang, Lbm study of aggregation of monosized spherical particles in homogeneous isotropic turbulence, Chem. Eng. Sci. **201**, 201 (2019).

[28] A. D. Bragg, P. J. Ireland, and L. R. Collins, Mechanisms for the clustering of inertial particles in the inertial range of isotropic turbulence, Phys. Rev. E **92**, 023029 (2015).

[29] A. D. Bragg and L. R. Collins, New insights from comparing statistical theories for inertial particles in turbulence: I. Spatial distribution of particles, New J. Phys. **16**, 055013 (2014).

[30] J. C. Brndle de Motta, W. P. Breugem, B. Gazanion, J. L. Estivalezes, S. Vincent, and E. Climent, Numerical modelling of finite-size particle collisions in a viscous fluid, Phys. Fluids **25**, 083302 (2013).

[31] H. Gao, H. Li, and L. P. Wang, Lattice Boltzmann simulation of turbulent flow laden with finite-size particles, Comput. Maths. Appl. **65**, 194 (2013).

[32] L. P. Wang, O. Ayala, H. Gao, C. Andersen, and K. L. Mathews, Study of forced turbulence and its modulation by finite-size solid particles using the lattice Boltzmann approach, Comput. Maths. Appl. **67**, 363 (2014).

[33] C. Peng, O. M. Ayala, and L. P. Wang, A direct numerical investigation of two-way interactions in a particle-laden turbulent channel flow, J. Fluid Mech. **875**, 1096 (2019).

[34] D. D'Humires, I. Ginzburg, M. Krafczyk, P. Lallemand, and L. S. Luo, Multiple-relaxation-time lattice Boltzmann models in three dimensions, Phil. Trans. R. Soc. Lond. A **360**, 437 (2002).

[35] V. Eswaran and S. B. Pope, An examination of forcing in direct numerical simulations of turbulence, Comput. Fluids **16**, 257 (1988).

[36] A. Caiazzo and M. Junk, Boundary forces in lattice Boltzmann: Analysis of momentum exchange algorithm, Comput. Math. Appl. **55**, 1415 (2008).

[37] A. Naso and A. Prosperetti, The interaction between a solid particle and a turbulent flow, New J. Phys. **12**, 033040 (2010).

[38] R. Zimmermann, Y. Gasteuil, M. Bourgoin, R. Volk, A. Pumir, and J.-F. Pinton, Rotational Intermittency and Turbulence Induced Lift Experienced by Large Particles in a Turbulent Flow, Phys. Rev. Lett. **106**, 154501 (2011).

[39] C. Lee, K. Yeo, and J. I. Choi, Intermittent Nature of Acceleration in Near Wall Turbulence, Phys. Rev. Lett. **92**, 144502 (2004).

[40] P. K. Yeung, S. B. Pope, A. G. Lamorgese, and D. A. Donzis, Acceleration and dissipation statistics of numerically simulated isotropic turbulence, Phys. Fluids **18**, 065103 (2006).

[41] A. G. Kidanemariam, C. Chan-Braun, T. Doychev, and M. Uhlmann, Dns of horizontal open channel flow with finite-size, heavy particles at low solid volume fraction, New J. Phys. **15**, 025031 (2013).

[42] F. Lucci, A. Ferrante, and S. Elghobashi, Modulation of isotropic turbulence by particles of taylor length-scale size, J. Fluid Mech. **650**, 5 (2010).

[43] J.-S. Ferenc and Z. Nda, On the size-distribution of poisson Voronoï cells, Physica A **385**, 518 (2007).